2014

Thermal Analysis of Phase Transitions in Perovskite Electroceramics

S. E. Young
Iowa State University, eliyoung@iastate.edu

H.Z. Guo
Iowa State University

C. Ma
Iowa State University

Matthew R. Kessler
Iowa State University, mkessler@iastate.edu

Xiaoli Tan
Iowa State University, xtan@iastate.edu

Thermal Analysis of Phase Transitions in Perovskite Electroceramics

Abstract
Perovskite oxide ceramics have found wide applications in energy storage capacitors, electromechanical transducers, and infrared imaging devices due to their unique dielectric, piezoelectric, pyroelectric, and ferroelectric properties. These functional properties are intimately related to the complex displacive phase transitions that readily occur. In this study, these solid-solid phase transitions are characterized with dielectric measurements, dynamic mechanical analysis, thermomechanical analysis, and differential scanning calorimetry in an antiferroelectric lead-containing composition, $Pb_{0.99}Nb_{0.02}[(Zr_{0.57}Sn_{0.43})_{0.92}Ti_{0.08}]_{0.98}O_3$, and in a relaxor ferrielectric lead-free composition, $(Bi_{1/2}Na_{1/2})_{0.93}Ba_{0.07}TiO_3$. The $(Bi_{1/2}Na_{1/2})_{0.93}Ba_{0.07}TiO_3$ ceramic develops strong piezoelectricity through electric field-induced phase transitions during the poling process. The combined thermal analysis techniques clearly reveal the differences in unpoled and poled ceramics.

Keywords
antiferroelectrics, lead-free, phase transition, thermal analysis, DSC, DMA, TMA

Journal of Thermal Analysis and Calorimetry 115, 587-593 (2014).
DOI: 10.1007/s10973-013-3363-1.

Thermal Analysis of Phase Transitions in Perovskite Electroceramics

S. E. Young, H. Z. Guo, C. Ma, M. R. Kessler, and X. Tan[a)]

Department of Materials Science and Engineering, Iowa State University, Ames, IA 50011, USA

Abstract Perovskite oxide ceramics have found wide applications in energy storage capacitors, electromechanical transducers, and infrared imaging devices due to their unique dielectric, piezoelectric, pyroelectric, and ferroelectric properties. These functional properties are intimately related to the complex displacive phase transitions that readily occur. In this study, these solid-solid phase transitions are characterized with dielectric measurements, dynamic mechanical analysis, thermomechanical analysis, and differential scanning calorimetry in an antiferroelectric lead-containing composition, $Pb_{0.99}Nb_{0.02}[(Zr_{0.57}Sn_{0.43})_{0.92}Ti_{0.08}]_{0.98}O_3$, and in a relaxor ferrielectric lead-free composition, $(Bi_{1/2}Na_{1/2})_{0.93}Ba_{0.07}TiO_3$. The $(Bi_{1/2}Na_{1/2})_{0.93}Ba_{0.07}TiO_3$ ceramic develops strong piezoelectricity through electric field-induced phase transitions during the poling process. The combined thermal analysis techniques clearly reveal the differences in unpoled and poled ceramics.

Keywords antiferroelectrics, lead-free, phase transition, thermal analysis, DSC, DMA, TMA

[a)]Author to whom correspondence should be addressed. E-mail: xtan@iastate.edu

Introduction

The demand for clean and renewable energy sources such as wind and solar requires efficient energy storage to ensure a consistent electrical energy supply. As electrical capacitors store energy directly as electrical charge, their efficiency and power density are ideal for this application; however, a typical electrical capacitor's energy storage density is far too low to allow practical, large scale implementation [1]. Lead-based antiferroelectrics that demonstrate a remarkably high energy storage density have been developed in the effort to bridge the gap between power density and energy density [2-4]. This is achieved through a reversible electrically induced phase transition between an antiferroelectric phase and a ferroelectric phase, resulting in the sudden development of high electrical polarization at the critical field of the phase transition [5-11]. During unloading of the capacitor, a large amount of electrical energy is released as the dielectric material reverts to an antiferroelectric state [2-4]. In simple terms, the dielectric properties of these materials are nonlinear with changing electric fields, and the utilization of nonlinear dielectrics in capacitors has the potential to create very high energy densities as long as sufficiently high electric fields are applied [4]. Of all the antiferroelectric ceramics the most widely studied compositions are lead zirconate titanate stannate doped with minor amounts of niobium or lanthanum [5-11]. In particular, $Pb_{0.99}Nb_{0.02}[(Zr_{0.57}Sn_{0.43})_{1-y}Ti_y]_{0.98}O_3$ (PNZST43/100y/2) shows promise for applications in high energy density capacitors because its antiferroelectric-ferroelectric transition can be easily manipulated and tuned [12,13].

Initially, $(Bi_{1/2}Na_{1/2})_{1-y}Ba_yTiO_3$ (BNT–100yBT) was designed as a lead-free piezoelectric composition [14,15]. It was speculated that these compositions exhibit an antiferroelectric state above the so-called thermal depolarization temperature [14] and their utilization in high-temperature capacitor applications was explored [16]. However, recently it was clarified that this

antiferroelectric phase is actually a relaxor ferrielectric phase [10,17,18]. The electrical poling process for the development of piezoelectricity not only aligns the domain polarization but also triggers complicated irreversible phase transitions [10,19].

Thermal analysis techniques were used to characterize various phase transitions and other properties in lead-containing and lead-free antiferroelectric and ferroelectric perovskites [20-28]. However, most of the previous work used only one particular technique. In the present study, a set of techniques, including dynamic mechanical analysis (DMA), zero-force thermomechanical analysis (TMA), and differential scanning calorimetry (DSC), were used to characterize the thermally induced phase transitions in ceramics of PNZST43/8/2, unpoled, and poled BNT–7BT. In addition, dielectric measurements and *in-situ* transmission electron microscopy (TEM) experiments were performed to complement and support the results of these thermal analyses.

Experimental

Materials

The antiferroelectric composition $Pb_{0.99}Nb_{0.02}[(Zr_{0.57}Sn_{0.43})_{0.92}Ti_{0.08}]_{0.98}O_3$ was synthesized using the solid state reaction method. Powders of PbO, ZrO_2, SnO_2, TiO_2, and Nb_2O_5 with purity levels exceeding 99.9% were batched with the addition of an extra 5 wt.% PbO to make up for the evaporation loss of lead during high temperature sintering. The batched powder was vibratory milled for 7 hours with zirconia media in ethanol, dried, pressed, and calcined at 935 °C for 4 hours. To ensure composition homogeneity, the described calcination process was repeated one more time. After milling for 15 hours, dried powder was uniaxially pressed with acrylic binder, and the resulting pellet was surrounded in protective powder of similar composition and sintered

at 1320 °C using a double crucible configuration. X-ray diffraction was used to ensure phase-purity of the sintered pellet. All reported measurements were performed on the same pellet.

$(Bi_{1/2}Na_{1/2})_{0.93}Ba_{0.07}TiO_3$ ceramic was also prepared with conventional solid state reaction using Bi_2O_3, Na_2CO_3, $BaCO_3$, and TiO_2 powders with purity levels exceeding 99.9%. Na_2CO_3 was baked at 200 °C for 15 hours to remove any moisture before batching. Calcination was carried out at 800 °C for 2 hours. After additional vibratory milling and drying, the powder was uniaxially pressed with polyvinyl alcohol binder and sintered at 1150 °C for 5 hours. X-ray diffraction was performed on the resultant ceramic to examine phase purity. Several BNT–7BT pellets were sintered because the planned experiments could be performed on unpoled and electrically poled samples. Electrical poling was conducted at room temperature under a DC field of 45 kV cm^{-1} for 15 minutes.

In addition to the compositions of interest, a pure $BaTiO_3$ sample was also prepared with $BaCO_3$ and TiO_2 powders as a means to calibrate the results between each of thermal analysis method. Calcination was conducted at 1100 °C for 6 hours and sintering at 1350 °C for 3 hours.

Dielectric, TEM, and thermal characterization

Dielectric constant and dielectric loss tangent of each composition were measured at 1 kHz, 10 kHz, and 100 kHz during heating from room temperature at a rate of 3 °C min^{-1}. The properties of the PNZST43/8/2 sample were measured in a temperature chamber with an LCZ meter (Model 3322, Keithley). A high temperature tube furnace with an LCR meter (Model 4284A, Hewlett Packard) was used to measure the BNT–7BT samples. The $BaTiO_3$ sample was measured with both setups.

To reveal the electric field-induced phase transition in BNT–7BT, the polarization vs. electric field hysteresis loop was recorded during the very first triangular wave cycle of field with a standardized ferroelectric test system (RT66A, Radiant Technologies). This phase transition was also visualized using the *in-situ* technique with a Phillips CM-30 microscope operated at 300 kV. Experimental details for the *in-situ* observation can be found in previous reports [29,30].

Prior to each thermal analysis experiment with PNZST43/8/2, the sample was cooled with dry ice for several hours to stabilize the ferroelectric phase. DMA measurement was carried out with a PerkinElmer DMA 7 at a 3 °C min^{-1} heating rate, using the 3-point bend mode with a 10 mm span, a 720 mN static force, and a 1 Hz 650 mN dynamic force. The sample was cut and polished to approx. 12 mm length, 4 mm width, and 0.5 mm thickness. For poled BNT–7BT sample, the poling field was applied along the thickness direction prior to the test.

Thermomechanical analysis was performed with a Q400 TMA from TA Instruments using a 5 mN static force and a 3 °C min^{-1} heating rate on each sample. For these measurements, samples were at least 6 mm tall, and the BNT–7BT sample was poled perpendicular to its height.

Finally, each sample was broken into ~20 mg pieces to perform DSC measurements (Model Q2000, TA Instruments) with a heating rate of 10 °C min^{-1}.

Results and discussion

PNZST43/8/2

The results of the dielectric analysis of PNZST 43/8/2 are displayed in Fig. 1(a). According to previous studies [6-9], the anomalies on the 1 kHz dielectric constant curve at 51, 140, and 172 °C mark the phase transitions from ferroelectric to antiferroelectric, to a multi-cell cubic

paraelectric, and then to a single-cell cubic paraelectric phase, respectively. Dielectric loss (tan δ) drops sharply at the ferroelectric to antiferroelectric transition (~51 °C), but shows no apparent changes at other transitions. The ferroelectric-antiferroelectric transition accompanies a change in volume, indicating a first order displacive transition [5]. The antiferroelectric to multi-cell cubic and subsequently to single-cell cubic transitions were thought to be two second order transitions [20]. In the base compound $PbZrO_3$, the antiferroelectric phase directly transforms to the paraelectric phase during heating. Incorporating Sn, Ti, and Nb in the chemical composition stabilizes an intermediate multi-cell cubic phase and replaces this first order transition with two second order ones [20].

Dynamic mechanical analysis of PNZST 43/8/2, shown in Fig. 1(b), reveals what appears to be a negative double-peak in storage modulus around the ferroelectric to antiferroelectric transition at 48 °C and 51 °C. From there, the ceramic experiences a dramatic elastic softening. When approaching the antiferroelectric to multi-cell cubic phase transition; its storage modulus drops from ~105 GPa to the lowest value of ~65 GPa at 137 °C. This is followed by a rapid increase in storage modulus to ~90 GPa at 153 °C, at which point it levels off and drops slightly until it reaches the multi-cell cubic to single-cell cubic transition at 166 °C and starts increasing again until it reaches ~115 GPa at 200 °C. The mechanical loss tangent is close to zero in the ferroelectric phase, but starts to increase at 45 °C, peaking at about 0.06 near 52 °C and then dropping slightly. The loss tangent peaks again at 0.07 at 128 °C and then drops gradually to about 0.02 at 149 °C, at which point it increases again and peaks at 163 °C. Above this temperature, the mechanical loss drops again, reaching nearly zero at 180 °C, remaining so in the single-cell cubic paraelectric phase. The mechanical loss tangent data indicates that there is a very limited ferroelastic activity in the ferroelectric phase, and the single-cell cubic paraelectric

phase behaves in an ideal elastic manner. The strong anelastic behavior in the antiferroelectric phase may have resulted from the large antiferroelectric domains in the microstructure that are also of ferroelastic nature [8,10].

Zero-force thermomechanical analysis of PNZST 43/8/2, shown in Fig. 1(c), reveals a large shrinkage of about 900 ppm (0.09%) when the ferroelectric phase transforms into the antiferroelectric phase. This corresponds to a 0.27% volume shrinkage; and its magnitude is comparable to that of volume expansion during the antiferroelectric to ferroelectric phase transition induced by the electric field [9]. The shrinkage began at 45 °C, its rate peaking at 48.5 °C, and leveling off at 54 °C. The two phase transitions at higher temperatures are just barely revealed by the TMA measurement in the form of a small increase in thermal expansion coefficient in the multi-cell cubic phase.

Differential scanning calorimetry of PNZST 43/8/2, shown in Fig. 1(d), produced similar results to previous experiments [23], revealing endothermic signals at each phase transition. The onset of the ferroelectric to antiferroelectric transition in this experiment is seen at 56 °C with a peak at 60 °C. The onset and peak temperatures for the antiferroelectric to multi-cell cubic transition are seen at 130 °C and 144 °C, respectively. A broad bump at ~174 °C was observed at the multi-cell to single-cell cubic transition.

The apparent discrepancy in the transition temperatures determined by DSC with respect to the other measurements may have been the result of the faster heating rate (10 °C min^{-1} vs. 3 °C min^{-1}) and/or an inaccuracy in the temperature calibration [31]. It should be noted that measurement differences between the different experimental techniques are quite common [24,25] and may also be related to the intrinsic physics of the transition [32]. The results shown in Fig. 1 confirm that the antiferroelectric-ferroelectric phase transition is of first order in nature

indicated by the abrupt decrease in dielectric loss tangent, sudden contraction in volume, and the presence of an appreciable DSC peak. The other two transitions were previously thought to be second order because of the gradual change in volume [20]. However, the present results seem to suggest that the antiferroelectric to multi-cell cubic transition is a first order transition indicated by its significant elastic softening and extremely sharp DSC peak.

BNT–7BT

It is known that BNT–7BT ceramics experience electric field induced phase transitions during poling [10,19,33]. This transition is revealed in Fig. 2 by the first cycle polarization vs. electric field hysteresis loop measurement. The inflection point on the loading segment in the first quadrant marks the relaxor ferrielectric to ferroelectric transition. The transition is irreversible at room temperature and the ceramic sample does not return to the relaxor phase with decreasing field. The *in-situ* TEM experiment shown in Fig. 3 further indicates the changes in crystal symmetry at the transition. In the unpoled state, BNT–7BT crystalizes in the *P4bm* symmetry with ferrielectric nanodomains, as shown in Fig. 3(a). Under the applied poling electric field, the grain in focus transforms to the *P4mm* symmetry, accompanied by the formation of large lamellar ferroelectric domains. The dramatic change in domain structure during electrical poling warrants a comparative study on unpoled and poled samples using thermal analysis techniques.

The dielectric measurement of unpoled BNT–7BT shown in Fig. 4(a) corresponds well to previous results [18]. The dielectric constant and loss tangent show a strong frequency dispersion in the *P4bm* phase with nanodomains. The frequency dispersion diminishes at approx. 180 °C. The peak at 262 °C, identified as T_m [14-16], and does not correspond to any structural phase

transition. The dielectric loss tangent starts to decrease at 100 °C and reaches its minimum value at approx. 180 °C. No anomaly is noticed at T_m in the loss tangent curve. The dielectric measurement of poled BNT–7BT in Fig. 5(a) shows a much reduced frequency dispersion up to 100 °C. This temperature is referred to as the thermal depolarization temperature, T_d, in literature [32] and marks the transition of the poling-induced ferroelectric phase to the relaxor phase. The dielectric loss tangent also peaks at this temperature. Beyond T_d, both poled and unpoled ceramics exhibit very similar dielectric behavior.

Both unpoled and poled BNT–7BT ceramics show a valley in storage modulus, see Fig. 4(b) and 5(b). For the unpoled ceramic, a broad valley occurs at 132 °C, accompanied by very little discernible change in mechanical loss tangent. In contrast, the poled ceramic's storage modulus shows a much sharper valley at 121 °C, accompanied by an obvious peak in mechanical loss tangent. The peak onset for the mechanical loss tangent lines up closely with the T_d at near 100 °C. The mechanical loss tangent has a value close to zero throughout the entire measurement temperature range for the unpoled ceramic, while it apparently exhibits higher values below the T_d peak for the poled ceramic, possibly attributable to the large ferroelectric domains in the poled ceramic.

Zero-force TMA reveals no visible change in the thermal expansion (~10 ppm $°C^{-1}$) of unpoled BNT–7BT from 25 °C to 400 °C (Fig. 4(c)). For the poled ceramic, Fig. 5(c) shows that the induced *P4mm* ferroelectric phase has a larger, varying thermal expansion coefficient from 25 °C to 100 °C. Near the T_d at 104 °C, the already negative slope of the thermal expansion coefficient drops further until it reaches nearly 0 ppm $°C^{-1}$ at 110 °C, at which point it increases again to level off near 10 ppm $°C^{-1}$ at 125 °C.

Differential scanning calorimetry results show no significant features in unpoled BNT–7BT, see Fig. 4(d). The heat flow for poled ceramic exhibits an abrupt change in slope at 87 °C, and an endothermic peak at 128 °C with an onset at 120 °C.

These results seem to suggest that unpoled BNT–7BT does not experience any structural phase transition in the temperature range measured (25 ~ 400 °C) because of its highly disordered nature. The anomalies in dielectric measurements may be associated with strain glass transitions [34]. When BNT–7B is poled, large ferroelectric domains are formed. The phase transition for the thermal disruption of these large domains at T_d appears to be a first order transition.

Conclusions

The combined thermal scan experiments determining dielectric constant and loss tangent, storage modulus and mechanical loss tangent, thermal expansion, and heat flow are very powerful in uncovering the nature of the complex phase transitions in perovskite oxides. Particularly, these experiments confirmed the first order nature of the ferroelectric to antiferroelectric and the antiferroelectric to multi-cell cubic transitions, and the second order nature for the multi-cell cubic to single-cell cubic transition in PNZST43/8/2. In the lead-free BNT–7BT, the dielectric anomalies are not accompanied by any structural transitions in the unpoled state. However, after electrical poling to a ferroelectric phase with large domains, the thermal depolarization process corresponds to a first order structural transition.

Acknowledgements This work was supported by the National Science Foundation (NSF) through Grant CMMI-1027873.

References

1. Basic research needs for electrical energy storage. U.S. DOE Workshop Report. 2007. http://science.energy.gov/~/media/bes/pdf/reports/files/ees_rpt.pdf. Accessed 14 Mar 2013.
2. Dougherty JP. Cardiac defibrillator with high energy storage antiferroelectric capacitor. US Patent 5545184. 1996.
3. Gachigi KW. Electrical energy storage in antiferroelectric-ferroelectric phase switching chemically modified lead zirconate ceramics. PhD dissertation, Penn. St. Univ. 1997.
4. Kwon S, Hackenberger W, Alberta E, Furman E, Lanagan M. Nonlinear dielectric ceramics and their applications to capacitors and tunable dielectrics. IEEE Electr Insul M. 2011;27(2):43-55.
5. Berlincourt D, Krueger H, Jaffe B. Stability of phases in modified lead zirconate with variation in pressure, electric field, temperature and composition. J Phys Chem Solids. 1964;25:659-74.
6. Viehland D, Forst D, Xu Z, Li J. Incommensurately modulated polar structures in antiferroelectric Sn-modified lead zirconate titanate: the modulated structure and its influences on electrically induced polarizations and strains. J Am Ceram Soc. 1995;78:2101-12.
7. He H, Tan X. Raman spectroscopy study of the phase transitions in $Pb_{0.99}Nb_{0.02}[(Zr_{0.57}Sn_{0.43})_{1-y}Ti_{0y}]_{0.98}O_3$. J Phys: Condens Matter. 2007;19:136003/1-13.
8. He H, Tan X. Electric field-induced transformation of incommensurate modulations in antiferroelectric $Pb_{0.99}Nb_{0.02}[(Zr_{0.57}Sn_{0.43})_{1-y}Ti_{0y}]_{0.98}O_3$. Phys Rev B. 2005;72:024102/1-10.

9. Frederick J, Tan X, Jo W. Strains and polarization during antiferroelectric-ferroelectric phase switching in $Pb_{0.99}Nb_{0.02}[(Zr_{0.57}Sn_{0.43})_{1-y}Ti_{0y}]_{0.98}O_3$ ceramics. J Am Ceram Soc. 2011;94:1149-55.
10. Tan X, Ma C, Frederick J, Beckman S, Webber K. The antiferroelectric ↔ ferroelectric phase transition in lead-containing and lead-free perovskite ceramics. J Am Ceram Soc. 2011:94;4091-107.
11. Tan X, Frederick J, Ma C, Jo W, Rödel J. Can an electric field induce an antiferroelectric phase out of a ferroelectric phase? Phys Rev Lett. 2010;105:255702/1-4.
12. Tan X, Frederick J, Ma C, Aulbach E, Marsilius M, Hong W, Granzow T, Jo W, Rödel J. Electric-field-induced antiferroelectric to ferroelectric phase transition in mechanically confined $Pb_{0.99}Nb_{0.02}[(Zr_{0.57}Sn_{0.43})_{1-y}Ti_{0y}]_{0.98}O_3$. Phys Rev B. 2010;81:014103/1-5.
13. Young SE, Zhang JY,Hong W, Tan X. Mechanical self-confinement to enhance energy storage density of antiferroelectric capacitors. J Appl Phys. 2013;113:054101/1-6.
14. Takenaka T, Maruyama K, Sakata K. $(Bi_{1/2}Na_{1/2})TiO_3$-$BaTiO_3$ system for lead-free piezoelectric ceramics. Jpn J Appl Phys. 1991;30(9B):2236-39.
15. Rödel J, Jo W, Seifert K, Anton EM, Granzow T, Damjanovic D. Perspective on the development of lead-free piezoceramics. J Am Ceram Soc. 2009;92:1153-77
16. Acosta M, Zang JD, Jo W, J. Rödel J. High-temperature dielectrics in $CaZrO_3$-modified $Bi_{1/2}Na_{1/2}TiO_3$-based lead-free ceramics, J Eur Ceram Soc. 2012;32:4327-34.
17. Ma C, Tan X. Phase diagram of unpoled lead-free (1-x)$(Bi_{1/2}Na_{1/2})TiO_3$-x$BaTiO_3$ ceramics. Solid State Commun. 2010;150:1497-500.
18. Ma C, Tan X, Dul'kin E, Roth M. Domain structure-dielectric property relationship in lead-free (1-x)$(Bi_{1/2}Na_{1/2})TiO_3$-x$BaTiO_3$ ceramics. J Appl Phys. 2010;108:104105/1-8.

19. Ma C, Guo HZ, Beckman SP, Tan X. Creation and destruction of morphotropic phase boundaries through electrical poling: A case study of lead-free $(Bi_{1/2}Na_{1/2})TiO_3$–$BaTiO_3$ piezoelectrics. Phys Rev Lett. 2012;109:107602/1-5.

20. Jaffe B, Cook WR, Jaffe H. *Piezoelectric Ceramics*. Adademic Press, Marietta. 1971.

21. De La Rubia MA, Alonso RE, DeFrutos J, Lopez-Garcia AR. Phase transitions in $PbTi_xHf_{1-x}O_3$ determined by thermal analysis and impedance spectroscopy. J Therm Anal Calorim. 2009;98:793-9.

22. Roy M, Dave P, Barbar SK, Jangid S, Phase DM, Awasthi AM. X-ray, SEM, and DSC studies of ferroelectric $Pb_{1-x}Ba_xTiO_3$ ceramics. J Therm Anal Calorim. 2010;101:833-7.

23. Yang P, Payne DA. Thermal stability of field-forced and field-assisted antiferroelectric-ferroelectric phase transitions in $Pb(Zr,Sn,Ti)O_3$. J Appl Phys. 1992;71:1361-7.

24. Wu C, Wang X, Yao X. Comparative study on the phase transitions in PZT-based ceramics by mechanical and dielectric analyses. Ceram Int. 2012;38S:S13-S16.

25. Zheng XC, Zheng GP, Lin Z, Jiang ZY. Thermal and dynamic mechanical analyses on $Bi_{0.5}Na_{0.5}TiO_3$-$BaTiO_3$ ceramics synthesized with citrate method. Ceram Int. 2013;39:1233-40.

26 Mendes SF, Costa CM, Sencadas V, Pereira M, Wu A, Vilarinho PM, Gregorio R, Lanceros-Méndez S. Thermal degradation of $Pb(Zr_{0.53}Ti_{0.47})O_3$/poly(vinylidene fluoride) composites as a function of ceramic grain size and concentration. J Therm Anal Calorim. 2013; doi:10.1007/s10973-012-2918-x.

27 Melo D, Marinho RMM, Vieira FTG, Lima SJG, Longo E, Souza AG, Maia AS, Santos IMG. Influence of Cu(II) in the $SrSnO_3$ crystallization. J Therm Anal Calorim. 2011;106:513-7.

28 Huang JW, Su P, Wu WW, Li YN, Wu XH, Tao L. Preparation of nanocrystalline $BiFeO_3$and kinetics of thermal process of precursor. J Therm Anal Calorim. 2013;111:1057-65.

29. Tan X, Shang JK. In-situ transmission electron microscopy study of electric field-induced grain boundary cracking in lead zirconate titanate. Phil Mag A 2002;82:1463-78.

30. Tan X, He H, Shang JK. In situ TEM studies of electric field-induced phenomena in ferroelectrics. J Mater Res. 2005;20:1641-53.

31. Mano JF, Lanceros-Mendez S, Nunes AM, Dionisio M. Temperature calibration in dielectric measurements. J Therm Anal Calorim. 2001;65:37-49.

32. Anton EM, Jo W, Damjanovic D, Rödel J. Determination of depolarization temperature of $(Bi_{1/2}Na_{1/2})TiO_3$-based lead-free piezoceramics. J Appl Phys. 2011;110:094108/1-14.

33. Daniels JE, Jo W, Rödel J, Jones JL, Electric-field-induced phase transformation at a lead-free morphotropic phase boundary: Case study in a $93\%(Bi_{0.5}Na_{0.5})TiO_3–7\%BaTiO_3$ piezoelectric ceramic. Appl Phys Lett. 2009;95:032904/1-3.

34. Yao Y, Yang Y, Ren S, Zhou C, Li L, Ren XB. Ferroelastic and strain glass transition in (1-x)$(Bi_{0.5}Na_{0.5})TiO_3$-x$BaTiO_3$ solid solution. EPL 2012;100:17004/1-5.

Fig. 1 Thermally induced phase transitions in polycrystalline PNZST 43/8/2 ceramic revealed by dielectric (a), DMA (b), TMA (c), and DSC (d) measurements.

Fig. 2 The polarization vs. electric field relation at room temperature measured at 4 Hz for the first cycle for unpoled BNT–7BT ceramic. Arrows illustrate the flow of time during the measurement.

Fig. 3 Electric field *in-situ* TEM results of a representative grain in BNT–7BT examined along the [112] zone-axis. Bright-field micrographs prior to application of poling field (a) and under a poling electric field (b). The direction of the poling field is indicated by the bright arrow in (b). The selected area diffraction patterns are shown in the insets. The presence of the 1/2{*ooe*} superlattice spots (one is highlighted by the bright circle in (a)) characterizes the *P4bm* symmetry.

Fig. 4 Temperature scan of dielectric property (a), storage modulus (b), thermal expansion (c), and heat flow (d) for unpoled BNT–7BT.

Fig. 5 Temperature scan of dielectric property (a), storage modulus (b), thermal expansion (c), and heat flow (d) for electrically poled BNT–7BT.

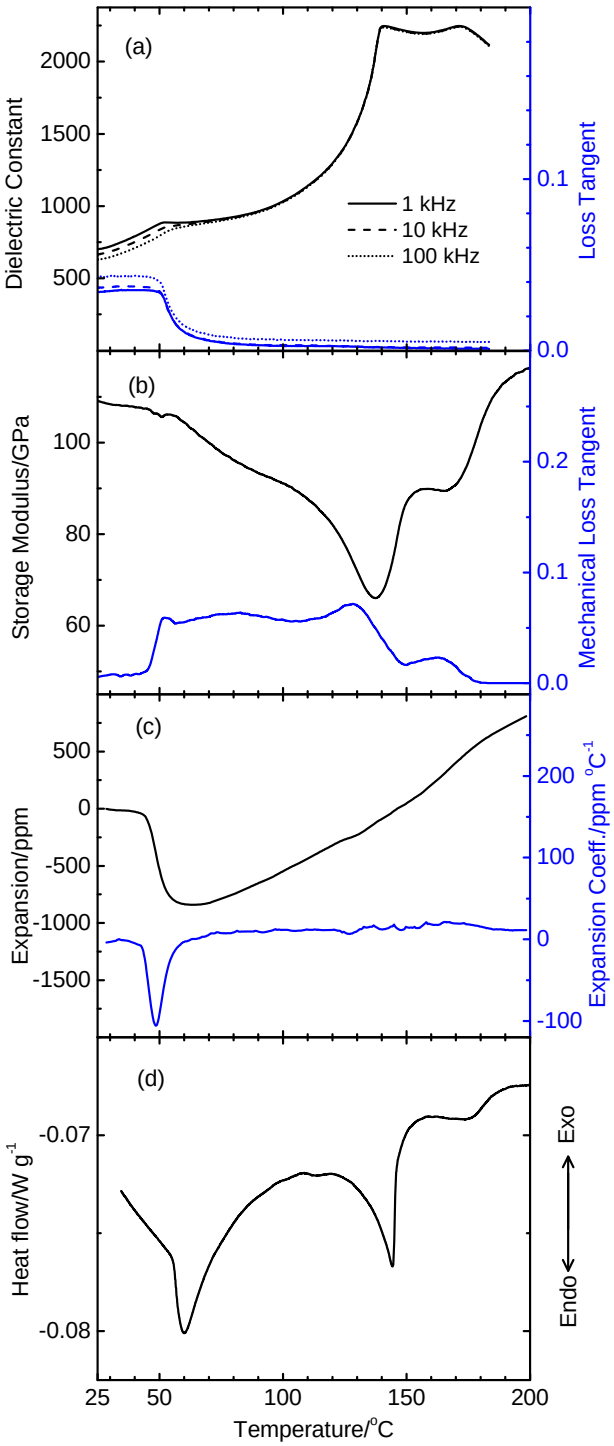
(a)
Dielectric Constant
2000
1500
1000
500
1 kHz
10 kHz
100 kHz
Loss Tangent
0.1
0.0
(b)
Storage Modulus/GPa
100
80
60
Mechanical Loss Tangent
0.2
0.1
0.0
(c)
Expansion/ppm
500
0
-500
-1000
-1500
Expansion Coeff./ppm °C-1
200
100
0
-100
(d)
Heat flow/W g-1
-0.07
-0.08
Exo
Endo
25
50
100
150
200
Temperature/°C

Fig. 1

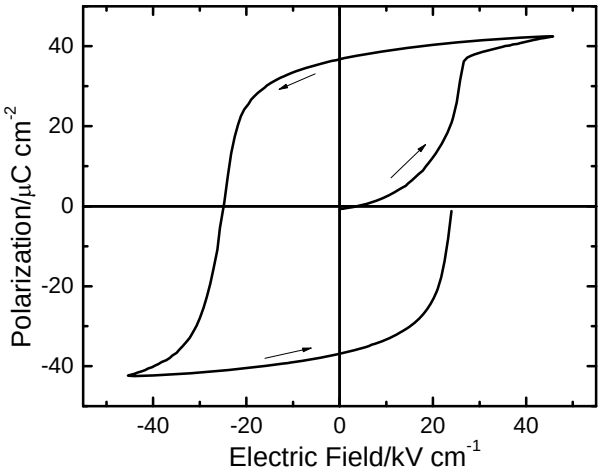
40
20
0
-20
-40
Polarization/μC cm-2
-40
-20
0
20
40
Electric Field/kV cm-1

Fig. 2

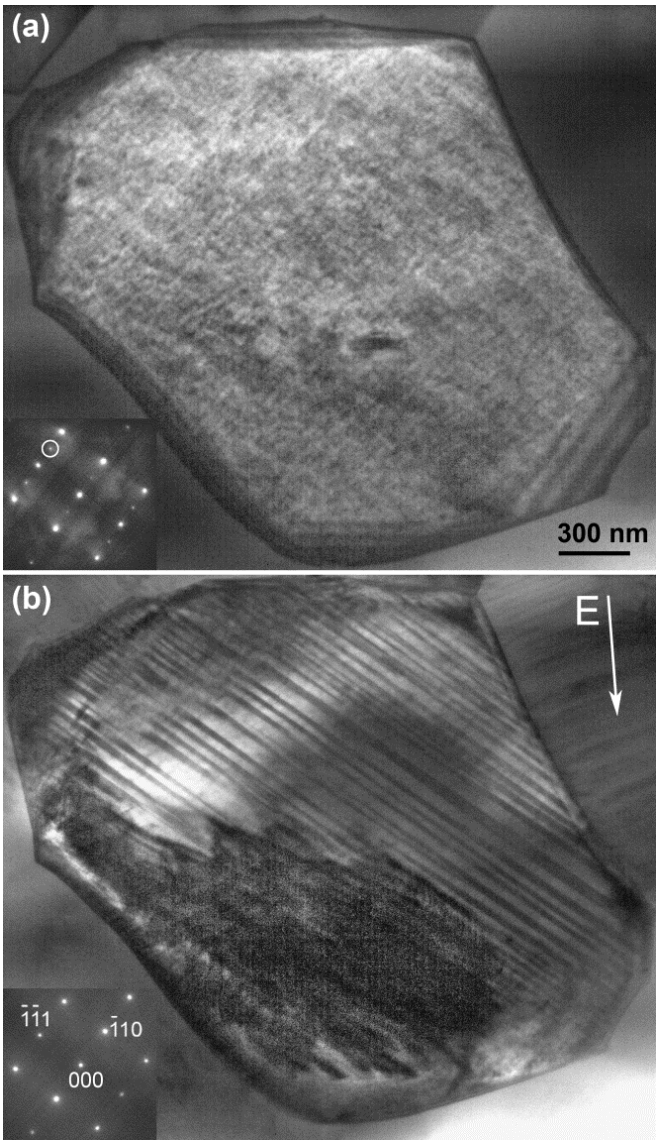

Fig. 3

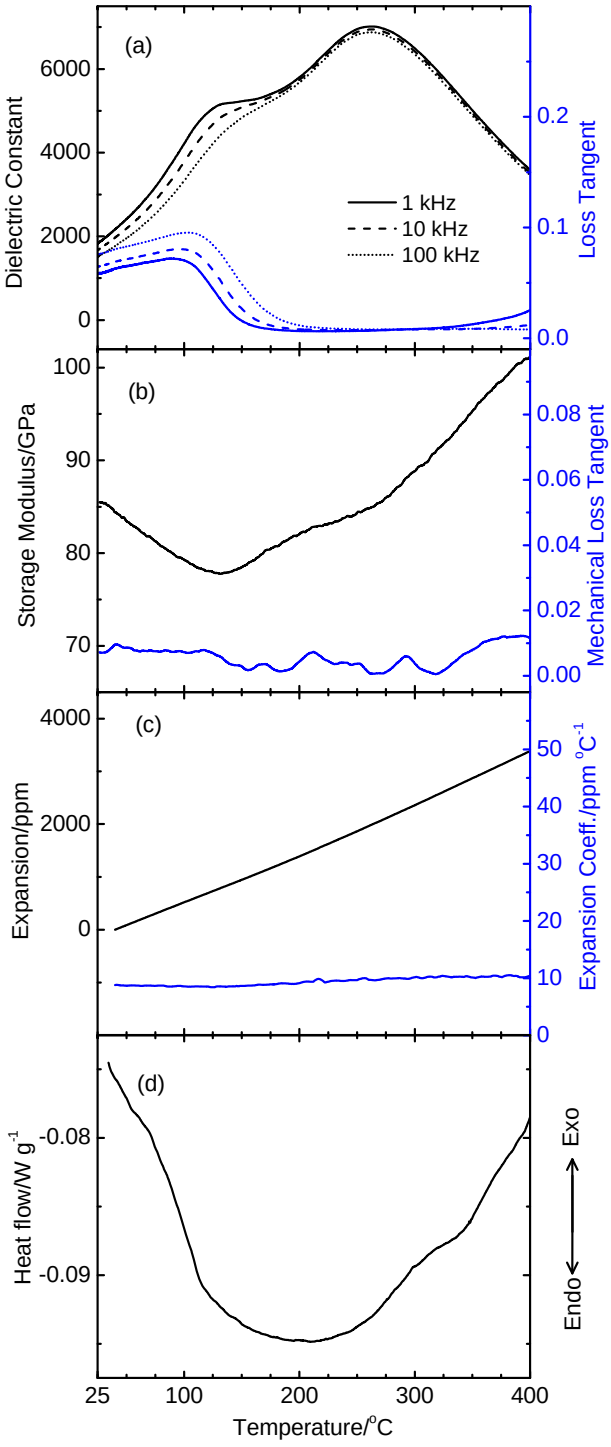
(a)
Dielectric Constant
Loss Tangent
1 kHz
10 kHz
100 kHz
(b)
Storage Modulus/GPa
Mechanical Loss Tangent
(c)
Expansion/ppm
Expansion Coeff./ppm °C-1
(d)
Heat flow/W g-1
Exo
Endo
Temperature/°C

Fig. 4

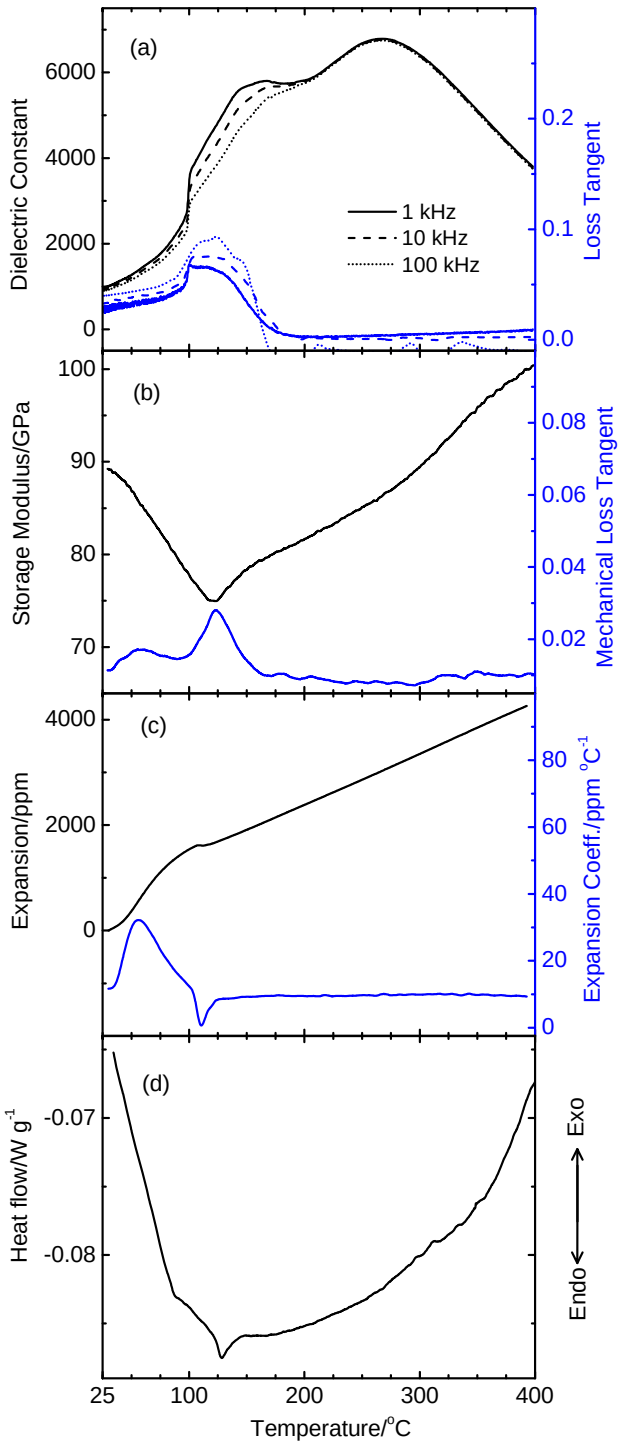
(a)
Dielectric Constant
Loss Tangent
1 kHz
10 kHz
100 kHz
(b)
Storage Modulus/GPa
Mechanical Loss Tangent
(c)
Expansion/ppm
Expansion Coeff./ppm °C-1
(d)
Heat flow/W g-1
Exo
Endo
Temperature/°C

Fig. 5